Integrated spatial and orientation analysis of quartz c-axes by computer-aided microscopy

RENÉE PANOZZO HEILBRONNER* and CHRISTIAN PAULI

Geological Institute, Bernoullistrasse 32, CH-4056 Basel, Switzerland

Abstract—A new method for the complete determination of quartz c-axis orientations is proposed. Its primary aim is to integrate the analysis of crystallographic orientations and the spatial distribution of the lattice orientations within the fabric in the form of high resolution AVA (Achsenverteilungsanalyse).

The method is based on standard mineral optics and image analysis techniques. It uses a slightly modified polarizing microscope, a surveillance camera and a computer (a universal stage is not necessary). The method has been developed for quartz but can be extended to the analysis of other uniaxial minerals.

The primary results of the analysis consist of three logical images which represent: (a) the azimuth and (b) the inclination of the c-axes, and (c) the goodness-of-fit of the analysis at every pixel. Thus, the absolute c-axis orientation is defined at each point of the picture, and can be displayed in colour-coded form (= AVA image). From the azimuth and inclination images, further results are derived. Transferring the orientations to a stereogram, a volume-weighted pole figure is obtained. By calculating the angular mismatch between pixels, i.e. by performing a gradient-filtering in orientation space, high- and low-angle grain boundaries are discriminated. As a consequence, image segmentation, i.e. the identification of grains and grain boundaries, is based on c-axis orientation and not on visual bias.

Simultaneous visualization of microstructure and crystallographic orientation greatly facilitates the analysis of deformation fabrics.

INTRODUCTION

IN structural geology, the determination of crystallographic fabrics plays an important role. The following methods are being used primarily: the 'classical' one which is based on the universal stage (Berek 1924), and a more recent one using the X-ray goniometer (e.g. Schmid et al. 1981). Results are usually displayed on equal-area stereograms (Schmidt 1925); and typical pole figure patterns are used to infer the type or mechanism of deformation, temperature conditions, etc. (e.g. Schmid & Casey 1986). X-ray goniometry has a few distinct advantages over the U-stage method. First, most crystallographic axes can be measured (or derived via the orientation distribution function), while optical measurements are restricted to c-axes. Second, the resulting pole figures are volume-weighted, and thirdly, data acquisition is computerized.

An alternative, less frequently adopted technique for analysing crystallographic fabrics is the so-called 'Achsenverteilungsanalyse' (analysis of distribution of axes, AVA) (e.g. Ramsauer 1941, Sander 1950). In order to carry out an AVA, the lattice orientations of a given sample are measured and plotted on a stereonet. On the pole figure, the lattice orientations are subdivided into a few important fields and assigned different colours. Finally, all grains of the microstructural framework are colour-coded according to their position in the pole figure. For this type of analysis, one has to use the U-stage because in X-ray goniometry the relation between the crystallographic orientation of a given grain and its

location on the thin section is not maintained. AVAs yield a very high quality of information, in the sense that crystallographic orientation and shape fabrics can be studied simultaneously. But, as is well known, to produce AVA images of reasonable size and resolution requires a great effort (e.g. Hobbs 1966, Knipe & Law 1987). Also, since the method is based on optical microscopy, only c-axes can be analysed.

Full crystallographic information and location can also be obtained by TEM (e.g. Fitz Gerald et al. 1983) and SEM electron channelling methods (e.g. Lloyd & Ferguson 1986). Thus, these methods would, in principle, permit the construction of AVAs for all crystallographic axes. However, due to specimen preparation, the areas of TEM specimens are usually very small. SEM specimens, on the other hand, can be as large as thin sections, but the procedure of obtaining and evaluating large numbers of electron channelling patterns (Lloyd & Freeman 1991), is also relatively time-consuming.

To relieve some of the tedium associated with U-stage work, various attempts have been made to automate some of the necessary manipulations or to substitute them altogether; the most elegant solution being offered by the photometric method (Price 1973). This method can be considered the optical equivalent of X-ray goniometry, in that it yields volume-weighted pole figures (Price 1980). By the same token it does not maintain the relation between the position of an individual grain and its c-axis orientation. An attempt has been made to approximate such a relation by analysing very small areas ('cells') (Price 1978).

Compared to the problem associated with finding the lattice orientation of a given grain, the problem of identifying the grain boundaries may seem minor. How-

---

*Also at: Department of Scientific Photography, Basel University, Basel, Switzerland.

ever, if we want to automatically analyse thin sections, the problem is not a trivial one, as is indicated by a large bulk of image analysis literature on the subject (for introduction see, e.g., Rosenfeld & Kak 1976, Gonzalez & Wintz 1977, Pratt 1978, Schalkoff 1989). A vast number of methods for image segmentation has been proposed. In general, they treat the image as a two-dimensional discrete brightness function, and the algorithms are based on finding certain characteristics (steps, gradients, constant grey-levels, etc.) in this distribution.

In general application, the brightness function of an image is the result of irradiation and absorption phenomena of the objects shown on the image, thus reflecting the geometry, colour and texture of the real world. In polarizing microscopy, the brightness function of a thin section image depends on the interference colours, and these in turn depend on the optical properties and crystallographic orientations of the mineral grains. Thus, the brightness function carries both geometrical (grain shape) and analytical (birefringence) information. From this point of view, thin section images may be considered as logical images, i.e. as images which display a physical information (lattice orientation), in colour-coded form. It is obvious, however, that the 'colour-coding' achieved by the polarizers and the lambda plate is not unique: any given interference colour corresponds to at least two distinct c-axis orientations.

The method presented here (called CIP, for computer-integrated polarization microscopy) combines the approach taken by Price with image processing methods (a parallel but maybe not as rigorous an attempt has been made by Beyna et al. 1990). The method is introduced in two parts: in the first part, the theoretical basis (optics and colorimetry) is presented. In the second part, the actual technique and procedures are demonstrated, and sample applications are discussed. Although the present paper is restricted to quartz, other uniaxial minerals can be analysed by the same technique. Biaxial minerals present a problem in so far as they have triaxial optical indicatrices, and hence their birefringence is not only a function of the inclination of the c-axis with respect to the thin section, but also a function of the orientations of the a- and b-axes. As a result, their interference spectra depend on two independent variables, the individual influences of which cannot be resolved by the method presented here. It is possible that minerals with nearly uniaxial optical properties could be analysed.

PART I: THEORETICAL BASIS OF METHOD

Optical principles

When viewing thin sections of minerals on the microscope under crossed polarizer conditions with the lambda plate inserted, we generally observe patterns of interference colours. Different grains have different colours depending on the birefringence of the mineral,
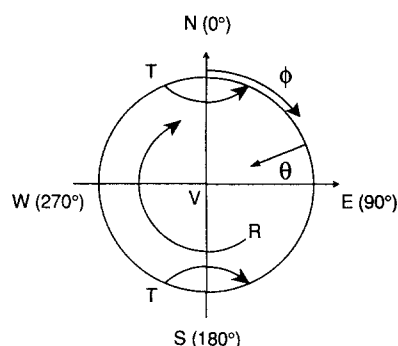

Fig. 1. Co-ordinate system and directions used in the paper. Lower-hemisphere, equal-area (Schmidt) projection. N, S, E, W: directions in plane of thin section. V: vertical axis. ϕ: azimuth; $0°$ in direction of N, increasing clockwise ($0° \leq \phi \leq 360°$). θ: inclination; $0°$ horizontal, in plane of thin section ($0° \leq \theta \leq 90°$). R: trajectory of clockwise rotation of c-axis. T: trajectory of west-down tilt of thin section.

the orientation of the c-axis and the section thickness. For example, on a thin section of 20–30 μm thickness, quartz grains, on account of their relatively low birefringence, will assume various shades of blue, yellow and first-order red.

Assuming that the polarizers are oriented N–S and E–W (Fig. 1), a quartz grain with its c-axis parallel to the N–S direction (azimuth, $\phi = 0°$, inclination, $\theta = 0°$) will appear first-order red. Rotating the stage 45° in a clockwise direction, the grain will turn blue, rotating to 90°, it will appear first-order red again. Increasing the rotation to 135° the grain appears yellow, and, finally, at 180° it will be first-order red again. During a complete revolution (of 360°), this colour sequence is repeated twice. If the inclination of the c-axis is increased ($\theta > 0°$), the colour contrast is reduced, in the sense that the blue and yellow hues are shifted towards first-order red, until, in the extreme case, when the c-axis is normal to the plane of the thin section ($\theta = 90°$), the grain appears a constant first-order red, irrespective of the azimuth. This is the one orientation that we can discriminate safely with the unaided eye; turning crystals into this orientation is one of the basic procedures when working with the U-stage.

If we imagine that we align the c-axis of a quartz grain parallel to all possible azimuths and all possible inclinations, and that we record on an equal-area stereonet the observed interference colours, we obtain a stereogram of interference colours (SIC) as shown in Fig. 2(a). Note that this stereogram has been generated numerically by calculating the interference spectra, $J(\lambda)$, for each position (ϕ, θ) of the stereonet and deriving the appropriate colour representation. The necessary equations and procedures are described in Appendices 1 and 2.

The optical equivalent of a SIC is the conoscopic image which is obtained by introducing the Bertrand lens in the microscope. Both the conoscopic image and the SIC depend on the birefringence of the mineral, the orientation of the optical axis, the thin section thickness and the optical properties of the lambda plate. Both may be considered as colour maps (or colour charts) which assign colours to c-axis orientations. However, because of their symmetry, the relation between colour and orientation is not unique, hence the inverse operation of

deriving the c-axis orientation from the interference colour is not possible. Each colour represents at least two, and in most cases four, possible orientations, and in the case of first-order red even an infinite number.

This phenomenon is well-known, and in optical microscopy it is, therefore, common practice to rotate the microscope stage (a procedure which reduces the symmetry of the information). On the SIC, the rotation of a c-axis is represented by a loop along a small circle (R trajectory of Fig. 1 superposed on Fig. 2a). For any given starting position a sequence of colours is traversed, corresponding to the colours that would be observed in the microscope. The angle of rotation necessary to encounter first-order red, for example, fixes the azimuth (between 0° and 180°), and the intensity of the colour contrast between the yellow and blue regions indicates the inclination. Provided that all colours, or colour sequences, can be distinguished sufficiently well from one another, a unique determination of the inclination (between 0° and 90°) is possible. The remaining problem is that we cannot differentiate between inclinations above ($\theta > 0°$) or below ($\theta < 0°$) the microscope table.

In order to overcome this ambiguity, the thin section has to be tilted, out of the plane of the microscope table. If we consider a west-down tilt of the thin section and two different c-axes with an initial inclination of 30° and initial azimuths of 0° and 180°, we find that the tilt produces a shift from first-order red to blue in the first case, and a shift towards yellow in the second case (compare T trajectories in Fig. 1). An analogous asymmetry could be produced by north-down tilts (about the east-pole). The *amount* of tilt is not critical, it is only required that the resulting change in colour be strong enough to be recognizable.

In principle, we have now assembled all the physical operations that are necessary for a unique derivation of c-axis orientations from a series of colour measurements.

Colorimetric considerations

The technical realization of the method requires that the measuring signal is converted from colour to monochrome, one reason being that we are not interested in colour itself but in the azimuth and inclination which it encodes. Moreover, since the proposed analysis is to be carried out for every pixel of the image, the input data should be as simple as possible.

The colour of interference spectra. To demonstrate the nature of the problem, we will briefly return to the physical basis of interference colours. A number of interference spectra of quartz have been calculated for various thin section thicknesses, for various orientations (ϕ,θ) and for a lambda plate that consists of quartz with a maximum extinction at 546 nm (Fig. 5). Turning a mineral grain whose c-axis lies within the plane of the thin section ($\theta = 0°$), from north towards east, the colours shift from first-order red (spectrum R), to the bluish hues of the first quadrant (spectra B1 and B2),

next to the yellowish hues of the second quadrant (Y1 and Y2). The stippled spectra (B2) and (Y2) show the influence of increasing the thin section thickness from 20 to 24 μm. If we place the c-axis parallel to the diagonals and increase the inclination, we obtain a blue-to-red (spectra B2–B3–R) or a yellow-to-red transition (spectra Y2–Y3–R).

In terms of visual perception, we do not see these spectra, we only react to the relative proportions of blue, green and red light, i.e. to the light intensities within the 400–500, 500–600 and 600–700 nm bands. For example, a light with an intensity maximum in the 600–700 nm range and only subdued intensity in the 400–500 nm range will appear yellow (spectra Y2 in Fig. 5).

Selection of the optimal filter. A very familiar way of converting colour to monochrome, i.e. of converting light of a given spectral composition into a single density value, is to use a black and white photographic film. The rendition of colours depends on the spectral sensitivity of the film, and in the case of a normal panchromatic film, it is not unlikely that many of the blue and yellow interference colours would be represented by identical grey values. In order to circumvent this problem, colour separation filters are used. The different effects of a Kodak Wratten filter No. 25 and of a narrow-band interference filter are demonstrated in Figs. 2(c) & (d). These monochrome SICs have been generated numerically, by calculating the interference spectrum at each co-ordinate point of the SIC, as before. Each spectrum is multiplied with the transmission curve of the respective filter (these curves are provided by the manufacturer), and the spectral intensities are summed. Finally, the resulting intensity distribution, $G(\phi,\theta)$, is scaled and displayed as an image where high intensities appear bright and low intensities dark. Pseudo-contour representations (obtained by bit-removing of the three most significant bits) are shown in Figs. 2(e) & (f).

Ideally, the filter should have the effect of producing a monochrome SIC with a grey value distribution, $G(\phi,\theta)$, approximating a hyperboloid surface. The absolute minima and maxima should occur at the periphery, and there should be a monotonic increase and decrease of minima and maxima towards the centre. Comparison of Figs. 2(c) and (d) shows that filter 25 (with an absorption edge at 600 nm) does not yield an optimal result (producing local minima *away* from the periphery), whereas the interference filter (transmitting at 700 nm) is a much better option.

On an optimally filtered SIC, the amplitude of the brightness function, $G(\phi)$, recorded along a 180° R trajectory (θ = constant) is uniquely defined by the inclination, θ, of the trajectory. Within 180°, each $G(\phi)$ should pass through one minimum and one maximum. Various versions of $G(\phi)$ along a trajectory at $\theta = 0°$ have been calculated assuming various filtering conditions (Fig. 6). Note that in the case of no filter, first-order red (which occurs at 0°, 90° and 180°) appears to be the darkest colour, whereas in the cases where red filters are used, the blue interference colours (in the orien-

tations around 45°) appear darkest and the yellow colours (around 135°) are brightest. For the given conditions (i.e. thin section thickness = 25 μm, Δn = 0.009, and a lambda plate of quartz with transmission minimum at 546 nm), the optimal choice would be the filter IF 700.

Once an optimal filter has been found, the function, $G(\phi)$, returns an amplitude and a phase. The phase angle, ϕ_{max}, where the maximum of the function, $G(\phi)_{max}$, occurs, yields the azimuth of the c-axis. The amplitude, i.e. the difference between $G(\phi)_{max}$ and $G(\phi)_{min}$, yields the inclination. The latter dependency, i.e. the amplitude as a function of θ, for constant ϕ, (denoted as Diff 25 or Diff 700 in Fig. 7), should decrease as linearly as possible with increasing inclination θ. However, for the filters that we have tested so far, we have not been able to make the slope of this function linear; in particular, the very shallow slope at high inclinations remains problematic.

Although the procedure of finding an optimal filter is one of trial and error, from the interference spectra of c-axes in the first and second quadrants one can estimate the appropriate filter wavelength. In the case of a 20 μm thin section, the maximum intensity difference between the yellow and the blue spectra occurs at 700 nm (solid spectra B2 and Y2 in Fig. 5). For thin sections that are thicker than 20 μm, the location of the optimal signal difference is outside the visible range, somewhere in the near infra-red region (stippled spectra B2 and B1 in Fig. 5). Because of the fact that many thin sections are thicker than 20 μm, we are using an infra-red sensitive camera. For filters that are not monochromatic, the spectral response of the recording equipment has to be included in the calculation.

Note that neither the grey value function, $G(\phi,\theta)$, of the monochromatic SIC, nor the grey value function along a rotation trajectory, $G(\phi)$, nor the functions $G(\theta)$ along transects of constant azimuth, are given in analytical form. They have to be calculated individually for any given set of birefringence, section thickness, camera, illumination, filter absorption, etc. In analysing the measured grey value signal, $G(\phi)$, we have used a simple $\sin^2$-fit, since the crucial point was finding the exact angle ϕ where the function $G(\phi)$ is a maximum, and finding the difference between $G(\phi)_{max}$ and $G(\phi)_{min}$, while the actual shape of the curve can be neglected.

Image processing and colour coding

For an image analysis approach it is essential that the image remains stationary. We therefore rotate the polarizers and the lambda plate while keeping the thin section fixed. In a series of images, the function $G(\phi)$ is recorded at each pixel (Fig. 8). Theoretically, the image should remain absolutely stationary, while the grey value at each pixel changes as a function of the rotation of the polarizers. If, however, the polarizers are mounted with a 4° tilt (which is often done to reduce reflections), small shifts of the image points may occur. Since the tilting operation also causes small shifts, and since there may be accidental shifts caused by manipu-

lations on the microscope, it is best to rematch and rectify the images prior to the actual analysis. The absolute orientation of the c-axis is then determined at all positions (pixels) of the image by extracting the amplitude and the phase from the $G(\phi)$ profiles, and by checking the tilt signal. The resulting azimuths and inclinations are scaled into 1 byte grey values and are stored in two image planes, as will be shown.

A final aspect concerns the representation of the results. We have adopted various methods of colour-coding the thin section, such that there is a unique relation between the colour of a given grain and the absolute orientation of its c-axis. A suitable colour-map is shown in Fig. 2(b), where every colour appears exactly once. On it, four c-axis orientations (20°/20°, 70°/20°, 200°/20° and 250°/20°), which would all appear an identical blue in the microscope, are assigned orange, yellow, light blue and dark blue. Although the choice of colours on the colour chart is arbitrary, one is limited by the readability of the resulting AVA. It may be useful to consider that similar directions should have similar colours. This presents a particular problem at the periphery of the stereographic colour map (Fig. 2a), where opposing edges correspond to parallel directions.

PART II: PRACTICAL APPLICATION

This part describes the equipment and procedures that we are using presently. It is focused on the analysis of quartz, but with the necessary adaptions (in particular, the necessary filter calculations), it can be used for other uniaxial minerals.

Equipment

We use a Zeiss Axioplan polarization microscope, with only minor modifications. In order to keep the image stationary with respect to the recording equipment, revolving polarizers are used. The lambda plate is mounted on the lower polarizer in the required 45° orientation. A standard illumination is used, but the infra-red absorbing filter is removed. The images are recorded using an Ikegami ICD-42E surveillance camera. This is a high sensitivity camera (0.01 lux) with infra-red response up to 800 nm. For the video capture we used the MediaGrabber of the RasterOps Color-Board 24STV, which is installed on a Macintosh IIfx. The colour simulation and filter calculation programs are written in Fortran and run on a Microvax workstation. The analysis proper is written in Pascal and runs on any Macintosh.

Data acquisition

For the proposed analysis, only high quality thin sections should be used. They should be polished on both sides and of constant thickness, at least over the area of interest. For quartz, the best thickness is 20 μm. The ideal filter is calculated and inserted. For the cases
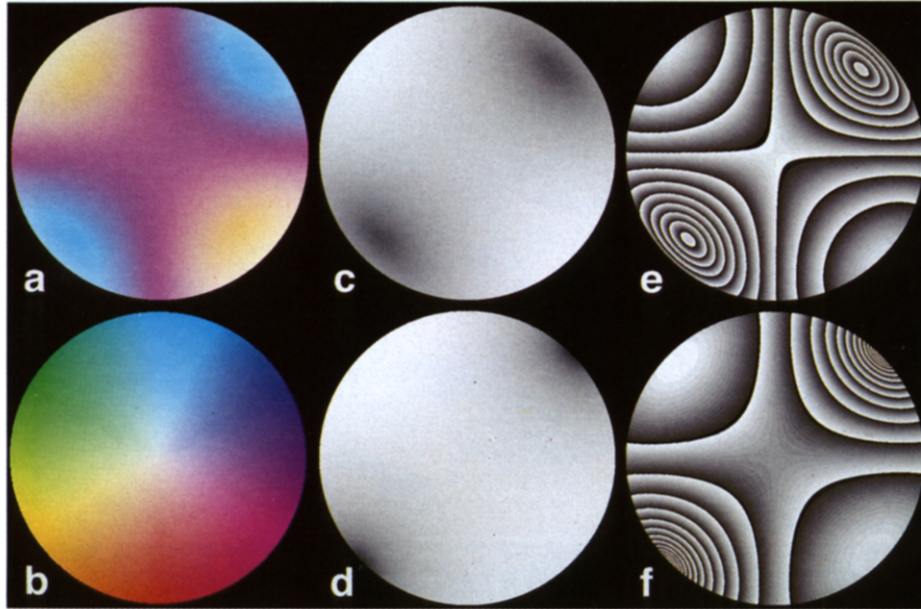
Fig. 2. Calculated stereograms of interference colours (SIC) and effect of monochromatic filtering. A thin section thickness of 20 μm is assumed. Lower-hemisphere, equal-area projections. (a) Interference colour is shown as a function of azimuth and inclination (ϕ,θ) of the quartz c-axis. Crossed polarizers and a lambda plate of gypsum with a maximum retardation at 550 nm are assumed (result is equivalent to conoscopic image). (b) Stereogram of colour code (colour-map): each orientation is represented uniquely by one colour. Hue (H) changes as a function of azimuth, saturation (S) changes as a function of inclination, while intensity (Y) is constant. (c) Monochromatic rendition of (a), calculated for Kodak Wratten filter No. 25. (d) Monochromatic rendition of (a), calculated for interference filter with maximum transmission at 700 nm. (e) Pseudo-contouring of (c) by significant-bit-removal (three most significant bits removed). (f) Pseudo-contouring of (d) by significant-bit-removal (three most significant bits removed).
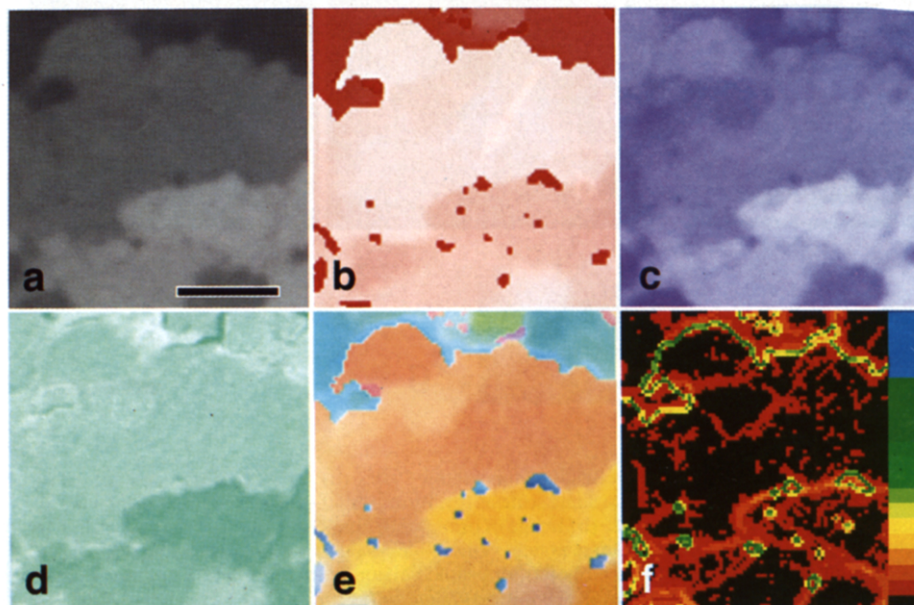

Fig. 3. Example of CIP analysis (specimen SP185 of Mancktelow 1990). (a) Monochrome image of $G(x,y)$ at azimuth $\phi = 0°$. Scale bar is 100 μm. (b) Colour-coded image of azimuth: full red = 360°, white = 0°. (c) Colour-coded image of inclination: full blue = 90°, white = 0°. (d) Colour-coded image of relative difference between curve-fit and measured values: full green = maximum difference, white = no difference. (e) AVA of same area (colour-code, see Fig. 2b). (f) Colour-coded image of orientation-based segmentation. Colour chart on right: black = no angular mismatch; red, orange = low-angle mismatch; yellow, green = high-angle mismatch.
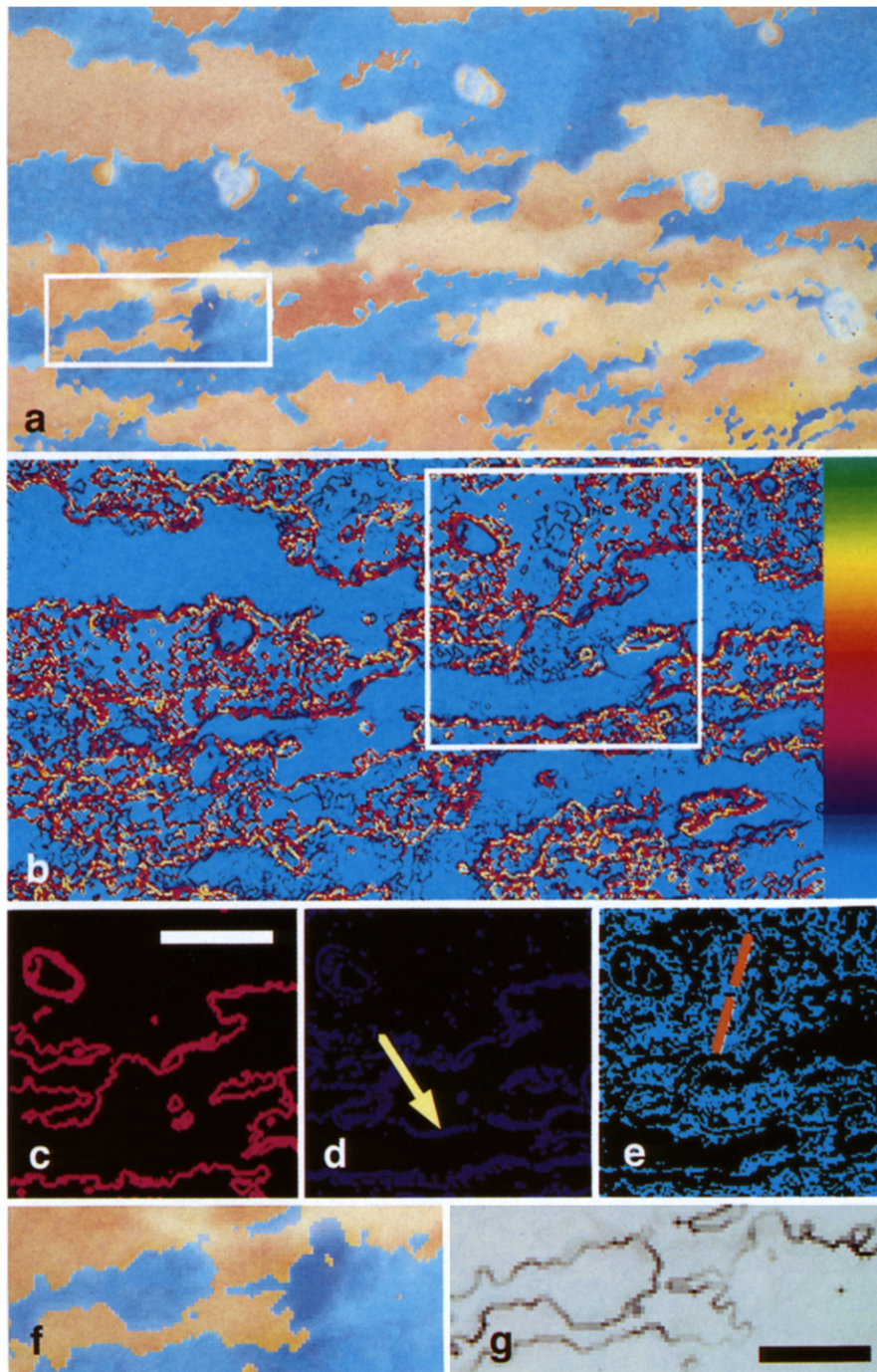
373

Fig. 4. CIP analysis of specimen SP178 (Mancktelow 1990). (a) AVA, colour-coded according to colour-code shown in Fig. 2(b). Same scale as (c). Inset: Bullet-hole stereogram, displaying all occurrences of c-axis orientations. (b) Image of orientation gradient. Colour-coding according to chart on right: blue = low-angular mismatch; yellow = high-angular mismatch. Same scale as (c). (c) Detail of framed area of (b): bitmap of threshold version of the orientation gradient image. Angular mismatch >8°. Scale bar is 100 μm. (d) Same as (c) for angular mismatch of 4–8°. (e) Same as (c) for angular mismatch of 2–4°. (f) Enlarged detail of framed area of (a). (g) Same area as (f): orientation gradient image (dark = high-angular mismatch). Scale bar is 50 μm.
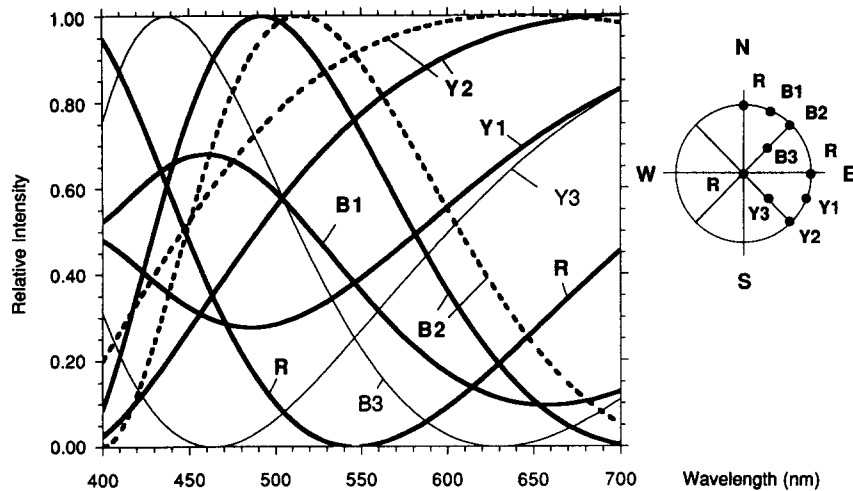
Fig. 5. Calculated spectra of interference colours J(λ) of quartz for crossed polarizer conditions and inserted lambda plate (quartz with a maximum extinction at 546 nm). The orientations of the c-axes of the spectra are shown on the little stereogram. Solid lines: thin section thickness is 20 μm. Broken lines: thin section thickness is 24 μm. Thin lines: inclination, θ, is 45°.

presented here, a monochromatic filter (from LOT GmbH manufacturers), transmitting at 701.6 ± 9.1 nm has been used. The thin section is mounted on the microscope table, and the first image is recorded. Next, the polarizers (including the lambda plate) are rotated in a counterclockwise sense (resulting in the clockwise rotation of the axes with respect to the polarizers). After each increment of 10°, a frame is recorded. This yields 18 frames for a 180° rotation. Four tilt operations are performed by placing matches below the long or short edges of the thin section slide, and the tilt images are recorded. The advantage of using several small tilts instead of one large one, is that only a minimal geometrical distortion of the image occurs.

It is of prime importance to record all images with a constant exposure (i.e. to turn off any type of automatic, internal correction which aims at a constant total image intensity for each frame). It is inevitable that fabrics with a strong preferred orientation will appear very dark in the blue orientation and very light in the yellow one. The

G(φ) curve would be completely ruined if the exposure were increased for dark orientations and reduced for bright ones.

Preprocessing

In the manner described above, a total of 22 images are recorded (Fig. 8). For a standard 640 × 480 size, roughly 7 Mbytes of storage space is required. The four tilt images are geometrically rectified using Image 1.43, a public domain image analysis program (Rasband 1992). For the very small tilts we are using (about 5° in any direction), the maximum pixel displacements are small, usually on the order of one or two pixels. The 18 untilted images also need some re-matching because of the differential wandering of image points as a function of c-axis orientation.

For the purpose of the numerical analysis, the relationship between recorded grey values and light intensities has to be well established. It is recommended
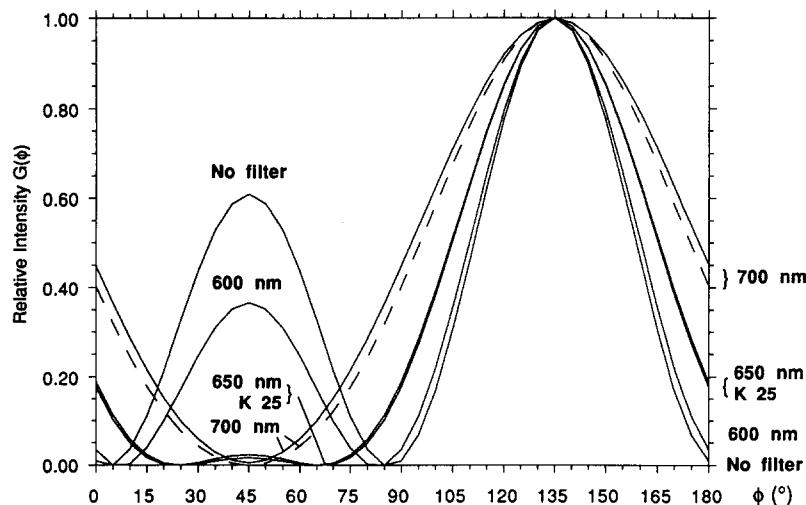

Fig. 6. Calculated grey value of interference spectra, G(φ), as a function of azimuth. Thin section thickness is 25 μm, inclination, θ, is 0°. No filter: using no filter. K 25: using Kodak Wratten filter No. 25. 600 nm: using monochromatic filter of 600 nm transmittance. 650 nm: using monochromatic filter of 650 nm transmittance. 700 nm: using monochromatic filter of 700 nm transmittance. Broken line: thin section thickness is 27 μm.
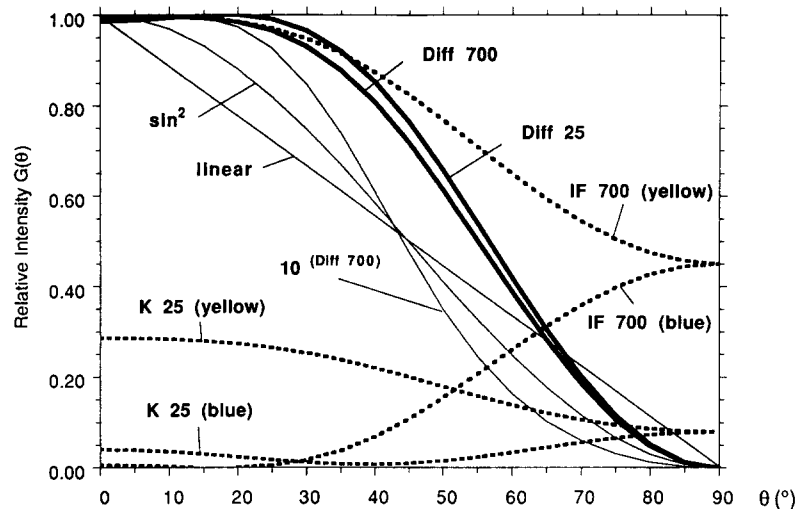
Fig. 7. The amplitude, $G(\phi)_{max} - G(\phi)_{min}$, of the grey value function as a function of inclination, θ. IF 700: using monochromatic filter transmitting at 700 nm. K 25: using Kodak Wratten filter No. 25. (blue) (yellow): grey value functions, $G(\theta)$ at $\phi = 45°$ $(G(\phi)_{min})$ or $\phi = 135°$ $(G(\phi)_{max})$. Diff: amplitude, $G(\phi)_{max} - G(\phi)_{min}$. sin²: sin²-function = theoretical grey value function under crossed polarizer conditions. $10^{(Diff\ 700)}$: for logarithmic input (see text).

the response curve of a given piece of recording equipment be determined, using a stepped transmission scale of optical densities (they are widely used in photographic densitometry). If the Gamma curve of the equipment cannot be modified in a suitable fashion, the images have to be preprocessed by correcting for contrast, or by adjusting the $G(\phi)$ and $G(\theta)$ curves (Figs. 6 and 7) accordingly. For our equipment, the appropriate signal curve is the $10^{(Diff\ 700)}$ curve shown in Fig. 7.

Derivation of the three primary images

The primary aim of the numerical analysis is to obtain the c-axis orientation of each pixel of the image. All other results (pole-figures, orientation maps, etc.) are derived from this. In other words, rather than first trying to identify individual grains (using standard image processing methods) and then carrying out one c-axis determination per grain, we *first* determine the c-axis orientation for each and every pixel, and *then* base the segmentation of the image on the c-axis orientations of the pixels (under normal circumstances segmentation is based on grey value variations). Both from a conceptual and from a practical point of view, this reversal has major advantages. The first practical consequence is that we achieve a significant data reduction in this matter. As will be shown, we can condense the information recorded in the 22 images into three. From these, a display of the absolute c-axis orientations in colour-coded form can be obtained (using, for example, the colour code shown in Fig. 2b). This corresponds exactly to an AVA image, with a maximum angular resolution. Next, the grain boundaries are found by calculating the angular differences between neighbouring pixels. In this manner, low- and high-angle boundaries can be separated, i.e. the whole spectrum of subgrain boundaries to grain boundaries can be differentiated. Such a differentiation would not be possible if the grain boundaries were derived on the basis of visual criteria, because the

relation between grey value contrast and angular mismatch is not unique. Note, however, that in the context of the CIP analysis, the definition of angular mismatch is based entirely on the misorientation of the c-axes. Lattice misorientations that affect the a-axes only remain undetected by this method. As a last result, because we do not only have one c-axis determination per grain, but one for every pixel, c-axes measurements may be used to create area-weighted pole figures, analogous to the ones obtained from ODF calculations (X-ray goniometry).

Geological context of selected specimens. The major steps of the c-axis analysis shall be introduced by way of two examples. We use thin sections made from quartz mylonites of the Simplon fault zone (SFZ). The regional geology of the SFZ, the c-axis pole figures and X-ray textures of many deformed quartz veins have been described and determined in detail by Mancktelow (1985, 1987, 1990). Two specimens, SP185 and SP178, were selected and will be used to test the method. They both come from the Simplon Pass area, where the deformation occurred under conditions of greenschist-facies metamorphism overprinting earlier amphibolite facies assemblages.

SP185 has been taken at some distance away from the Simplon Line itself. Its texture is kinematically consistent with the movement along the line, its microstructure however is coarse grained and shows domains of 40–500 μm size grains aligned in a fabric of quartz ribbons that are up to a few cm long (see appendix C, specimen No. 14, of Mancktelow 1990). Figure 3 shows a part of SP185 that is approximately 300 μm wide.

SP178 (specimen No. 25, of Mancktelow 1987 and 1990) was collected from a strongly deformed quartz vein near the Simplon Line itself. Its c-axes (determined with the U-stage) lie on a slightly kinked single girdle (see appendix D, specimen No. 25, of Mancktelow 1990). The microstructure consists of elongate to ribbon-shaped 'old grains', with a dispersed develop-

ment of elongate subgrains and new grains of an average grain size of approximately 80 μm. A shape fabric due to elongate subgrains, new grains and asymmetric grain boundary bulges is developed. The processed frame (shown in Fig. 4) has a long dimension of about 600 μm and represents only a small part of the thin section and therefore contains only a part of the elements of the c-axis texture, as will be shown.

Based on the colour simulations described above, and estimating the thickness of the thin sections to be 20 μm, an interference filter of 700 nm transmittance was used.

Calculation of phase angle and amplitude. The images which record the grey value function $G(x,y)$ at 18 rotational increments are considered first. For each pixel, the images yield 18 measuring points of the grey value

function $G(\phi)$. As a general approximation to the shape of the $G(\phi)$ curves, the program fits a sin^2-function to these points. The exact functional form of the approximating function is not critical, it is only required that the function should have a well-defined maximum and minimum such that we may derive a unique value for the amplitude and one for the phase angle. An obvious source of error for this curve-fit is the overlap of two adjacent grains, whether it is a real overlap in the thin section (oblique grain boundaries) or one that is due to differential wandering of image points.

The amplitude, i.e. the intensity difference $G(\phi)_{max} - G(\phi)_{min}$, is stored in a first image file. The maximum possible value is 255. From the phase angle of rotation, ϕ_{max} (= angle of $G(\phi)_{max}$), a preliminary azimuth ($\phi = \phi_{max} - 135°$) is calculated. The corresponding image is
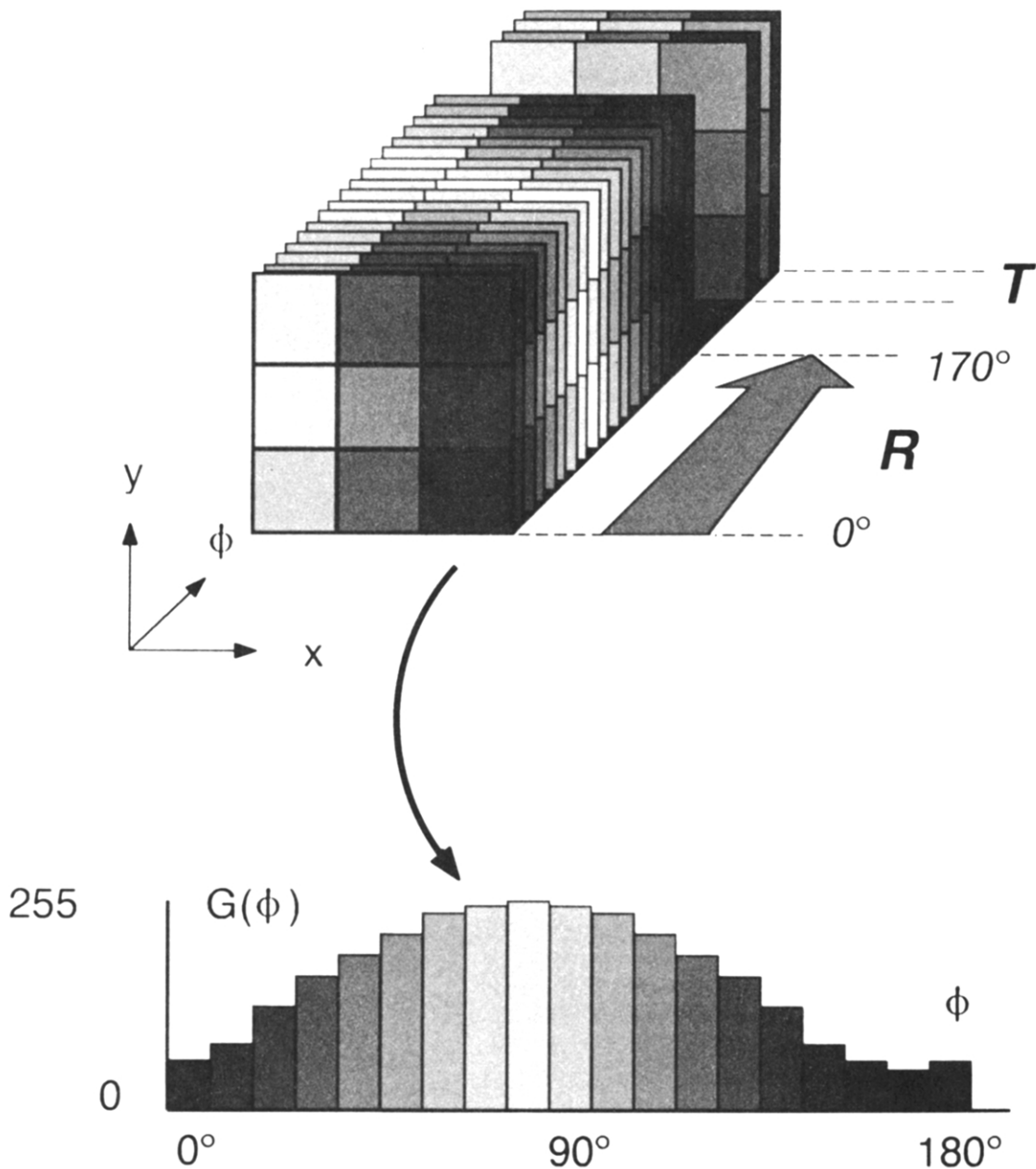

Fig. 8. Schematic representation of 22 image planes. R: 18 images for rotations. T: four images for tilt operations. x,y: co-ordinates of image plane. ϕ: angle of rotation. $G(\phi)$: grey value as a function of rotation, for constant θ, and for constant x and y (= grey value of one pixel). $G(x,y)$: two-dimensional grey value as a function of x and y (= image at given angle of rotation).

stored in a second image file. At this point, the maximum integer value that can occur is 179, since we determine the azimuth only in the range between 0° and 179°.

Calculation of inclination. The conversion of amplitude to inclination depends on the calibration of the recording equipment. Ideally, the original recordings should be in terms of intensities, and the derived amplitudes should be converted to inclination values by using the appropriate $G(\theta)$ curve, which, in our case, is the curve denoted $10^{(\text{Diff } 700)}$ in Fig. 7. As a first approximation, however, we have used a linear conversion. As a consequence, there is a tendency for underestimating shallow inclinations, and overestimating higher ones.

Further problems arise when the *c*-axis orientations cluster around a single maximum, or when in the area of analysis there are no shallow inclinations. In such cases, the range of values of derived amplitudes spans only a part of the curve shown in Fig. 7, and, without an absolute external standard or calibration the correlation between amplitude and inclination is very difficult. In addition, when recording in the infra-red, stray-light plays an important role. There is a tendency for dark pixels in an overall bright image to be overexposed. In fabrics with a strong preferred *c*-axis orientation this may cause serious underestimations of the amplitude of the $G(\phi)$ curves for dark grains.

With regard to the problems associated with the determination of the inclination, the following improvement is suggested. Using circular polarization (i.e. inserting $\lambda/4$ retarders above and below the thin section), a further image is recorded, using white light or monochromatic light in the visible region (e.g. 550 nm). The azimuth is unimportant because, under conditions of circular polarization, the brightness depends on inclination only, the relation between the two is again a $\sin^2$-function (consider Equation A1 of Appendix 1). Since the grey level does not depend on azimuth, the term that describes the dependence on ϕ may be set constant, and the $\sin^2$-dependence on inclination, θ, is given implicitly by substituting equation (A4) into equation (A1), and keeping λ at a fixed value. This procedure may replace the inclination determination from the $G(\phi)$ curves or it may be used to calibrate (i.e. double check) the derived amplitudes. In any case, the rotation and tilt images are still necessary to obtain the correct azimuth.

Calculation of azimuth. In order to obtain the true azimuth of every pixel, the first of the rotation images $(G(x,y)$ at $\phi = 0°)$ is compared to the four tilt images. If the sequence of grey levels becomes brighter, the tilt must cause the *c*-axis to wander into a yellow quadrant, if it becomes darker, it wanders into a blue one. From this, and the preliminary azimuth, one can determine whether the true azimuth is equal to the preliminary one or whether it has to be augmented by 180°.

Calculation of goodness-of-fit. The difference between the curve-fit and the measured values of $G(\phi)$ is

stored in a third file. This serves as a quality control, and as an indicator of the precision that can be expected from the analysis. It is obtained by calculating, for each pixel, the differences between the measured $G(\phi)$ values and the corresponding values of the $\sin^2$ curve-fit. The 18 differences are added and normalized with respect to the amplitude of the $G(\phi)$ curve.

We may assume that, in some cases, the large values in the difference image may point to the fact that the mineral in question is not quartz, and in particular that the optical indicatrix is biaxial.

Presentation of results

Primary images. As an example, the CIP analysis of specimen SP185 will be discussed. Figure 3(a) shows a subarea (of 300 μm width) of the first of the 18 rotation images. The grey values depend on the *c*-axis orientations of the pixels, but pixels that have identical grey values at this particular azimuth may still have different *c*-axis orientations. The result of the CIP analysis is stored in three image planes. The first one is a record of the azimuth (Fig. 3b), the second one of the inclination (Fig. 3c), and the third one of the difference between the measured values and the curve-fits (Fig. 3d).

As of now, we have based the description of orientation on 360° of azimuth and 90° of inclination. To represent the azimuth with a 1° resolution, we ought to have an image depth of 9 bits. This, however, causes some inconveniences when the image is to be displayed, because most image processing software assumes an image depth of 1 byte (=8 bits). Thus, we have scaled the range of 360° into the available 256 integer values, thereby creating 1.4° intervals. Since the range of inclinations is only 90°, there is no problem in representing all angles to one degree increment. For better accuracy it is suggested that the *c*-axis orientations be stored with an azimuth range of 0–180°, and that the tilt information be used to correct the *inclination* file such that it spans a range from $-90°$ to $+90°$. In this manner, a 1° resolution of orientation can be achieved for both angles.

For the derivation of the azimuth, the quality of the thin section polish is critical. Surface asperities may cause the tilt signals to fluctuate locally, yielding opposite senses from one pixel to the next. On the azimuth image (Fig. 3b), the values run from 0° (white) to 360° (fully saturated red). In the lower half, we may note a large area of nearly constant azimuth, and in it, small areas of contrasting orientation. The angular difference between the small areas and the surrounding large grain(s) is 180°. Since there is no corresponding contrast in the inclination image (Fig. 3c), we may be certain that these little areas are artefacts. Note that while the maximum colour contrast is at 360°, the maximum contrast in orientation is at 180°. As a consequence, very high visual contrasts may be misleading: while the azimuth contrast may be very high, the angular difference (e.g. between 1° and 359°) may be small.

In the inclination image, low inclinations are white, high inclinations blue. Thus, the small grains that were

noted above and the surrounding larger one, which all appear very light, have a more or less constant, low inclination. It is very unlikely that the little areas represent small subgrains which are parallel to each other and exactly 180° contrary to the surrounding grain. Furthermore, we have noted similar small areas, at many other sites within this thin section. They occur preferably in grains of low inclination. On the basis of the strong contrast between these areas and the host grains, such artefacts are removed easily by standard image processing methods.

The goodness-of-fit is also represented as a logical image (Fig. 3d). Small differences, i.e. good curve-fits, are represented by less saturated green hues, larger differences by more saturated ones. Visually, the difference appears inverse to the inclination image (compare Figs. 3c & d). The light-green grains of good curve-fit coincide with the dark-blue grains of high inclination. The goodness-of-fit appears to be a function of inclination, possibly because the image noise introduced by the poor polish is noticed most in grains of low c-axis inclination. On the difference image, grain boundaries which are more or less normal to the plane of the thin section have a tendency of showing up as white lines. Their $G(\phi)$ curves are very nearly constant because vertical grain boundaries appear black at all rotational increments. Oblique grain boundaries, on the other hand, show higher errors and therefore appear darker. (The signal derived from two overlapping grains deviates very noticeably from the $\sin^2$ curve-fit.)

AVA images. From the azimuth and inclination images, the absolute orientation of each pixel is calculated. In order to display this information as an AVA image, the colour-map shown in Fig. 2(b) has been used. On it, hue indicates the azimuth and saturation indicates inclination. The resulting AVA is shown in Fig. 3(e). From the colour of any pixel on the AVA image, the absolute c-axis orientation can be inferred. Pixels with very saturated colours have c-axes which are parallel or closely parallel to the plane of the thin section whereas whitish pixels represent areas where the c-axes are more nearly normal to the plane of the thin section. Various areas of opposing hue can be detected. The most noticeable ones are the little areas of failed tilt correction discussed above. Further such areas are revealed by the little magenta-coloured spots that are situated within larger areas of green grains, near the top of the figure.

Grain boundary detection. The absolute c-axis orientations of the pixels can be represented by vectors. Since a grain is defined as a volume of nearly constant crystallographic orientation, neighbouring pixels with parallel orientation vectors belong to one grain. As in all optical analysis, there is some ambiguity left, since two neighbouring grains could have parallel c-axes and differ only on account of their a-axis orientations. The angular difference (gradient) between the c-axis orientation of any two neighbouring pixels can be easily calculated. If it is zero, there is no boundary. If the difference is small,

we have the site of a subgrain boundary. If it is large, we have a grain boundary. To obtain a gradient image that is independent of direction, we calculate for each pixel the sum of the angular differences between its c-axis and that of its four nearest neighbours. The resulting image is shown in colour-coded form (Fig. 3f). Consistent with parallel c-axis orientations of the pixels, the interior of grains are shown as black areas of zero gradient. High-angle boundaries are shown by bright yellow and green colours, low-angle boundaries are shown by red and orange pixels. Obviously, the small areas of failed tilt correction show up as high-angle boundaries. A very nice example of a subgrain which is outlined in red by a low-angle boundary is depicted in the upper left quadrant of the figure; the corresponding subgrain is barely detectable on the AVA image (see Fig. 3e). To the right of this subgrain is an area of small segments of low-angle boundary. These could be due to noise or they could represent a smeared-out grain boundary. From inspection of the processed versions of the primary azimuth and inclination images, one can deduce that this area is one of gradual orientation change. Thus, we may note that, on account of a more transitional change of c-axis orientation, low-angle boundaries may be several pixels wide, moreover, they may be so spread out as to remain undetected by the gradient filter.

If we think in terms of a profile across a given boundary, we note that the total angular mismatch between the adjacent grains is obtained by integrating the mismatches of each pixel over the width of the grain boundary. High-angle boundaries are usually only one to two pixels wide. Although they are often bordered by zones of low gradient pixels, most of the angular mismatch is concentrated along the center of the boundary. As a consequence, it is often much more difficult to detect low-angle boundaries than high-angle ones, because, in addition to representing a weak signal, low-angle boundaries tend to be less localized than high-angle ones.

Orientations of c-axes. In order to discuss c-axis orientations, we will consider specimen SP178. The AVA image (Fig. 4a) has been obtained by the same colour-coding as the previous one. An area of approximately $600 \, \mu m$ width is shown. The most striking feature (apart from the little blobs which represent glue drops) is the layering of elongate grains or ribbons with alternating c-axis orientation. The inset pole figure shows all occurrences of c-axis orientation; it is not volume-weighted. It reveals the orange and blue orientation as co-planar, but of opposing inclination (point symmetry of stereogram). The glue drops, although disturbing the aesthetics of the image, have proved to be very useful for the matching operations that were necessary in the course of preprocessing the images.

When trying to trace the grain boundaries along the contrast between blue and orange areas, we have to keep in mind that low c-axis inclinations tend to create misleading visual contrasts. Since the azimuths of pixels whose c-axes are nearly parallel but inclined above and

below the plane of thin section come out 180° apart, fully saturated colours from opposing edges of the colour-map are juxtaposed: orange and blue as in the case mentioned above. Although the visual contrast is at a maximum, the angular mismatch is very small.

One could therefore apply other colour-maps, in particular, maps that have the *less* saturated colours at the periphery. This would create a more gradual colour transition for pixels that have low inclinations, but opposing azimuths. Having fixed colour-maps, i.e. maps that are stationary with respect to the E–N–V co-ordinate system (Fig. 1) of the stereogram, permits an easy comparison among different fabrics. On the other hand, one could envisage that the colour coding should be problem-oriented, in the sense that it should be adapted to the particular fabric in question. For example, a fully saturated colour could be centered where the c-axis maximum occurs.

The segmentation of SP178 is shown by the gradient image (Fig. 4b). It is given in colour-coded form using the colour chart indicated on the right. Over most of the image, sites of high gradient (brightly coloured pixels) coincide with high colour contrast in the AVA image. The framed rectangular area has been analysed in greater detail. Using the technique of grey level slicing, three ranges of gradient values have been selected, corresponding to various angular mismatches. Pixels with an angular mismatch of more than 8° form very well defined grain boundaries (Fig. 3c). The same grain boundaries are traced out by pixels that have an angular mismatch of between 4° and 8° (Fig. 4d), and these in turn are traced out by the pixels of 2–4° mismatch (Fig. 4e). This demonstrates the gradual change of orientation at the grain boundary. (Part of this gradual nature, however, may be an artefact of the method.) In Fig. 4(d), a low-angle boundary is clearly depicted (arrow). In Fig. 4(e), two dashes highlight a zone of concentrated occurrence of boundary segments. This area corresponds to an edge of undulous extinction that can be seen quite clearly in the AVA image. Using images such as these, and applying eroding and dilating operations, one could obtain (on an interactive basis) continuous tracings of various classes of grain boundaries and subject them to separate shape analysis. Thus, one would be able to analyse preferred orientations of subgrain boundaries separately from grain boundaries, etc.

Returning to the AVA image and its colour contrast, we note that for the fabric presented here, the orientation of the c-axis with respect to the plane of the thin section is such that the orange–blue colour contrast of the AVA image almost always coincides with a grain boundary on the gradient image. However, there are exceptions, e.g. Figs. 4(f) & (g). The latter depicts gradients in a simple black and white contrast: high-angle mismatches are dark, contiguous grains are light. The angular mismatch associated with a grain boundary may change, and even disappear, along the grain boundary (see Fig. 4g, near the scale bar). Comparing these two images, we note that the colour contrast persists
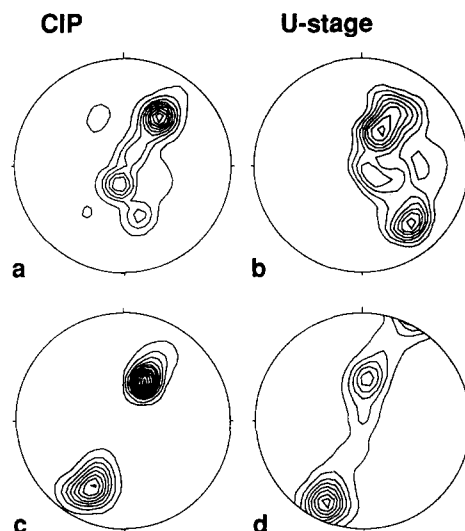

Fig. 9. Comparison of calculated pole figures of quartz c-axes and U-stage measurements for specimens SP185 and SP178. (a) Pole figure of CIP analysis of SP185. (b) Pole figure of U-stage measurements of SP 185. (c) Pole figure of CIP analysis of SP178. (d) Pole figure of U-stage measurements of SP178.

even if the gradient apparently drops to zero. This is related to the colouring artefacts discussed previously. We therefore recommend the use of a segmentation image, rather than relying on the AVA image alone.

Since we have the full orientation of all pixels (stored in the azimuth and inclination images), we may produce c-axis pole figures. We have obtained the pole figures for SP185 and SP178 using the program "StereoPlot" by Mancktelow (1989). For specimen SP185 we have performed a separate U-stage measurement of the selected specimen area. The comparison is shown in Figs. 9(a) & (b) and 10(a) & (b). Note two isolated maxima on the left side of the stereogram. They are artefacts created by the failed tilt correction discussed previously, and should be rotated about 180°. Further discrepancies arise because the image co-ordinate system is rotated about 10° with respect to the thin section co-ordinates. The most noticeable difference, however, stems from the fact that one very large grain at roughly 40° azimuth is expressed very strongly on the CIP pole figure, but not on the U-stage pole figure.

For the comparison of pole figures of SP178, we must consider that the area of evaluation used for the U-stage measurements (Mancktelow 1990) and that used for the CIP method do not coincide. The layer of SP178 that we have selected is not representative of the entire fabric, in that it has only very few grains of high c-axis inclination (under crossed polarizers with the lambda plate inserted, the selected area of the thin section is almost entirely blue). This absence of high inclinations shows up very nicely in the derived stereogram (compare Figs. 9c & d and 10c & d). A slightly wedge-shaped distribution of c-axes can be seen, it also shows up in the inset stereogram of Fig. 4(a). Stray-light effects have a tendency to produce wedge-shaped clusters but through a separate evaluation (using the U-stage), we have confirmed this distribution. With respect to geological co-ordinates, this means that the orientation variation of

the c-axes is indeed greatest for orientations that approach the xz-plane.

Evaluation of method

Spatial resolution. The spatial resolution and the reproducibility of the three primary images and of the AVAs depend on several factors, most notably: the mechanical stability of the microscope and the recording equipment; the quality of the optical system; image magnification; and the obliquity of grain boundaries (as described above). Another important influence is due to the fact that all image points rotate on small circular paths as the polarizers are rotated. On the image, the radius of the circular path depends both on the magnification and on the inclination of the c-axis. Thus, the image points pertaining to grains of different inclination will be displaced with respect to each other. And as a consequence, the grain boundaries are shifted too. Subtracting the first from the last image, the shifts are expressed as steps in a pseudo-relief, and the width of the steps can be taken as a measure of the spatial resolution. Another point worth considering is the size of the filters. The median filter which is applied to the azimuth and the inclination images is a square $3 \cdot 3$ filter. For the cases discussed here, the estimated reproducibility is within 3 pixels.

Orientational resolution. Provided that a given thin section is well polished, the results of azimuth calculations are within 5° of the corresponding U-stage measurements (Figs. 10a & c). The precision of the

inclination determination depends on the c-axis orientation distribution. If the distribution is such that the entire range of inclinations between 0° and 90° is present in the fabric, the amplitudes of the $G(\phi)$ curves can be calibrated 'internally'. If, however, the c-axes form a single maximum, only a partial spectrum of inclinations can be recorded, and an 'external' or absolute calibration is necessary. It is expected that once the equipment is calibrated, the precision of inclination determination will also be within 5° of the U-stage measurements. Thus, we should expect the orientation determinations by the method presented here to be as good as those by U-stage measurements. (It is outside the range of this paper to speculate on the precision of U-stage measurements.)

SUMMARY

The method presented combines polarizing microscopy and image analysis techniques. It enables a complete analysis of c-axis orientation without using a U-stage. It has been presented for the analysis of quartz. The analogous implementation for other uniaxial minerals is more or less straightforward.

The following results are obtained.

(1) Three logical images (primary images) are created which contain azimuth and inclination of each pixel, and a goodness-of-fit.

(2) Colour coding of the absolute orientation yields true AVA images.

(3) Evaluation of ϕ and θ values of all pixels yields a volume-weighted stereogram (which is easier to compare to X-ray goniometry than non-weighted U-stage stereograms).

(4) Images are segmented by calculating the angular mismatch between pixels. Large angular mismatches between pixels, i.e. high-angle boundaries, yield bright edges; low angular mismatches, i.e. subgrain boundaries, yield dark edges.

(5) Once the boundaries are found, their geometry can be studied. By differentiating between high- and low-angle boundaries, surface orientations of grain and subgrain boundaries can be determined independently. The relation between grain shape and c-axis orientation can be studied for each individual grain.
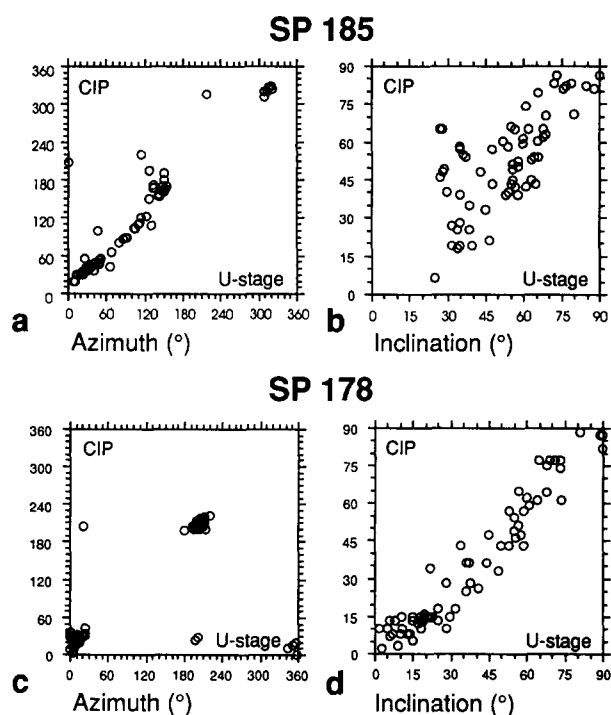

Fig. 10. Comparison of c-axis orientations obtained by the CIP method and by U-stage measurements. (a) Specimen SP185: CIP azimuth vs U-stage azimuth. (b) Specimen SP185: CIP inclination vs U-stage inclination. (c) Specimen SP178: CIP azimuth vs U-stage azimuth. (d) Specimen SP178: CIP inclination vs U-stage inclination.

REFERENCES

Bartels, J., Borchers, H., Hansen, H., Hellwege, K.-H., Schäfer, K.

& Schmidt, E. (editors) 1962. *Landolt-Börnstein, Zahlenwerte und Funktionen*. 2. *Band*, 8. *Teil: Optische Konstanten*. Springer, Berlin.

Berek, M. 1924. *Universaldrehtischmethoden*. Berlin.

Beyna, G., Leymarie, P., Buffet, G. & Nault, L. 1990. Principe de l'analyse des fabriques d'axes C du quartz par le traitement d'images numeriques. *C. r. Acad. Sci., Paris, Ser. II* **310**, 1233–1239.

Burri, C. 1950. *Das Polarisationsmikroskop*. Verlag Birkhäuser, Basel.

Clarke, D. & Grainger, J. F. 1971. *Polarized Light and Optical Measurement*. Pergamon Press, Oxford.

Fitz Gerald, J. D., Etheridge, M. A. & Vernon, R. H. (1983). Dynamic recrystallization in a naturally deformed albite. *Textures & Microstruct.* **5**, 219–237.

Gonzalez, R. C. & Wintz, P. 1977. *Digital Image Processing*. Addison-Wesley, Reading, Massachusetts.

Hobbs, B. E. 1966. Microfabric of tectonites from the Wyangala Dam Area, New South Wales, Australia. *Bull. geol. Soc. Am.* **77**, 685–706.

Knipe, R. J. & Law, R. D. 1987. The influence of crystallographic orientation and grain boundary migration on microstructural and textural evolution in an S–C mylonite. *Tectonophysics* **135**, 155–169.

Lloyd, G. E. & Ferguson, C. C. 1986. A spherical electron-channelling pattern map for use in quartz petrofabric analysis. *J. Struct. Geol.* **8**, 517–526.

Lloyd, G. E. & Freeman, B. 1991. SEM electron channelling analysis of dynamic recrystallization in a quartz grain. *J. Struct. Geol.* **13**, 945–953.

Mancktelow, N. S. 1985. The Simplon Line: a major displacement zone in the Western Lepontine Alps. *Eclog. geol. Helv.* **78**, 73–96.

Mancktelow, N. S. 1987. Quartz textures from the Simplon fault zone, SW Switzerland and N Italy. *Tectonophysics* **135**, 133–153.

Mancktelow, N. S. 1989. StereoPlot for Macintosh, version 1.1.

Mancktelow, N. S. 1990. The Simplon fault zone. *Beitr. geol. Karte Schweiz, N.F.* **163**.

Pratt, W. K. 1978. *Digital Image Processing*. John Wiley & Sons, New York.

Price, G. P. 1973. The photometric method in microstructural analysis. *Am. J. Sci.* **273**, 523–537.

Price, G. P. 1978. Study of heterogenous fabric and texture within a quartz–feldspar mylonite using the photometric method. *Bull. geol. Soc. Am.* **89**, 1359–1372.

Price, G. P. 1980. The analysis of quartz-*c*-axis fabrics by the photometric method. *J. Geol.* **88**, 181–195.

Ramsauer, H. 1941. Achsenverteilungsanalysen an Quarztektoniten. Unpublished dissertation, University of Innsbruck, 1–26.

Rasband, W. 1992. Image 1.43. National Institute of Health, Research Services Branch NIMH.

Rosenfeld, A. & Kak, A. C. 1976. *Digital Picture Processing*. Academic Press, New York.

Sander, B. 1950. *Einführung in die Gefügekunde der geologischen Körper, zweiter Teil: Die Korngefüge*. Springer, Wien.

Schalkoff, R. J. 1989. *Digital Image Processing and Computer Vision*. John Wiley & Sons, New York.

Schmid, S. M. & Casey, M. 1986. Complete fabric analysis of some commonly observed quartz *c*-axis patterns. *Am. Geophys. Un. Geophys. Monogr.* **36**, 263–286.

Schmid, S. M., Casey, M. & Starkey, J. 1981. An illustration of the advantages of a complete texture analysis described by the orientation distribution function (ODF) using quartz pole figure data. *Tectonophysics* **78**, 101–117.

Schmidt, W. 1925. Gefügestatistik. *Schweiz. miner. petrogr. Mitt.* **38**, 392–423.

Wyszecki, G. & Stiles, W. S. 1982. *Color Science* (2nd edn). John Wiley & Sons, New York.

APPENDIX 1
CALCULATION OF INTERFERENCE SPECTRA

Given a set of crossed polarizers whose primary directions are parallel to the N–S and E–W directions, and a thin section placed in between the two, the spectrum of light intensity, $J(\lambda)$, can be calculated according to the following equation, which is attributed to Fresnel (for details of derivations see, e.g. Burri 1950):

$$J(\lambda) = J_o(\lambda) \cdot \sin^2(2\Psi) \cdot \sin^2(\pi/\lambda \cdot R), \qquad (A1)$$

where J_o is the original intensity, Ψ is the azimuth between the optical axis of the crystal and the polarizer, R is the relative optical path-length difference and λ is the wavelength. R depends on the thickness, d, of the thin section and on the birefringence, Δn,

$$\Delta n(\lambda) = n_e(\lambda) - n_o(\lambda), \qquad (A2)$$

where n_e and n_o are the refractive indices of the extraordinary and the ordinary ray, respectively. Since the refractive index of the extraordinary ray depends on the angle, δ, between the wave normal and the optical axis, the general formulation of the relative optical path length difference is as follows:

$$R = R(\lambda) = d \cdot (n'_e(\lambda) - n_o(\lambda)), \qquad (A3)$$

where n'_e is the refractive index of the extraordinary ray under the condition of oblique incidence. For rays parallel to the optical axis of uniaxial minerals, n'_e is equal to n_o, for rays normal to the optical axis, n'_e is equal to n_e. For oblique incidence, i.e. for a given angle δ between the wave normal and the optical axis, n'_e may be calculated as follows

$$(1/n'_e(\lambda))^2 = (\cos(\delta)/n_o(\lambda))^2 + (\sin(\delta)/n_e(\lambda))^2. \qquad (A4)$$

Note that in standard polarizing microscopy, the optical axis of the microscope and the directions of the polarizers are set up such that Ψ is equal to ϕ, while δ is equal to $90° - \theta$. For quartz, which is a positive uniaxial mineral, $n_e(\lambda) > n_o(\lambda)$, with $n'_e(\lambda)$ decreasing from 1.55813 (at 397 nm) to 1.54049 (at 707 nm) (values taken from Landolt & Börnstein—see Bartels *et al.* 1962). To obtain a continuous function that describes the dependence of n_e, n_o or Δn as a function of λ, a Cauchy approximation may be used:

$$n(\lambda) = A + B/\lambda^2 + C/\lambda^4 + \dots . \qquad (A5)$$

Fitting measured values of Δn of quartz between 300 and 900 nm (data taken from Landolt & Börnstein—see Bartels *et al.* 1962 and Clarke & Grainger 1971), we obtain $A = 8.71 \times 10^{-3}$, $B = 1.30184 \times 10^2$ and $C = 1.3252361 \times 10^6$, if the wavelength, λ, is measured in nm.

If a lambda plate is inserted, the situation becomes more complex. Equation (A1) has to be generalized from a situation in which one mineral is placed between the crossed polarizers to one in which there are two (after Burri 1950, p.137):

$$
\begin{aligned}
J(\lambda)/J_o(\lambda) = \\
-\sin(2(\Psi_1 - \Psi_2)) \cdot \sin(2\Psi_1) \cdot \cos(2\Psi_2) \cdot \sin^2(\pi/\lambda \cdot R_1(\lambda)) \\
+\sin(2(\Psi_1 - \Psi_2)) \cdot \cos(2\Psi_1) \cdot \sin(2\Psi_2) \cdot \sin^2(\pi/\lambda \cdot R_2(\lambda)) \\
+\cos^2(\Psi_1 - \Psi_2) \cdot \sin(2\Psi_1) \cdot \sin(2\Psi_2) \cdot \sin^2(\pi/\lambda \cdot [R_1(\lambda) + R_2(\lambda)]) \\
-\sin^2(\Psi_1 - \Psi_2) \cdot \sin(2\Psi_1) \cdot \sin(2\Psi_2) \cdot \sin^2(\pi/\lambda \cdot [R_1(\lambda) - R_2(\lambda)]), \quad (A6)
\end{aligned}
$$

where Ψ_1 is the azimuth of the optical axis of the mineral in the thin section, and Ψ_2 the azimuth of the optical axis of the lambda plate. R_1 and R_2 are the relative optical path-length differences, of the mineral and of the lambda plate, respectively. For the standard set-up, the slow direction of the lambda plate (i.e. the direction of n_y) is invariably 45°, thus, Ψ_2 is 45°, and equation (A6) can be simplified.

APPENDIX 2
CALCULATION OF RGB VALUES FROM INTERFERENCE SPECTRA

To the human eye an interference spectrum appears as a colour. On the computer monitor, the colour is recreated by modulating the red, green and blue beams that hit the red, blue and green fluorescent dyes of the screen. Depending on the software by which colour is displayed on the screen a number of different colour systems may be used. We have chosen to calculate the RGB values. The simple option is to integrate the intensities from 400 to 500 nm, from 500 to 600 nm, and from 600 to 700 nm for the blue, green and red channels, respectively. As a general rule, these colours are slightly undersaturated. The result may be improved by visually adapting the saturation of the channels. The alternative option is to calculate the three RGB values by multiplying the interference spectrum with the three NTSC curves of the blue, green and red screen phosphors respectively (for details see, e.g. Wyszecki & Stiles 1982). Depending on the quality of the monitor, minor corrections may still be necessary.